PHYSICAL REVIEW RESEARCH **5**, 013115 (2023)

Electron acceleration by laser plasma wedge interaction

S. Marini,[1,2] M. Grech,[3] P. S. Kleij,[2] M. Raynaud,[2] and C. Riconda[1,*]

[1]*LULI, Sorbonne Université, CNRS, CEA, École Polytechnique, Institut Polytechnique de Paris, F-75252 Paris, France*
[2]*LSI, CEA/DRF/IRAMIS, CNRS, École Polytechnique, Institut Polytechnique de Paris, F-91128 Palaiseau, France*
[3]*LULI, CNRS, CEA, Sorbonne Université, École Polytechnique, Institut Polytechnique de Paris, F-91120 Palaiseau, France*

(Received 14 February 2022; accepted 10 January 2023; published 15 February 2023; corrected 17 March 2023)

An electron acceleration mechanism is identified that develops when a relativistically intense laser irradiates the wedge of an overdense plasma. This induces a diffracted electromagnetic wave that carries a significant longitudinal electric field and that accelerates electrons from the plasma over long distances to relativistic energies. Well collimated, highly charged (nC) electron bunches with energies up to hundreds of MeV are obtained using a laser beam with $I\lambda_0^2 = 3.5 \times 10^{19}$ Wμm^2/cm^2. Multidimensional particle-in-cell simulations, supported by a simple analytical model, confirm the efficiency and robustness of the proposed acceleration scheme.

DOI: 10.1103/PhysRevResearch.5.013115

I. INTRODUCTION

The interest in developing novel compact energetic particle and radiation sources via ultraintense laser-plasma interaction mechanisms has steadily increased over the last decade as they are useful for a large variety of applications ranging from image generation [1] to proton therapy [2], passing through space propulsion [3]. With this aim, various schemes were proposed and studied in detail, either involving the broad category of laser wakefield acceleration [4] or the interaction of a laser with an overdense plasma [5–24], in which our work is inscribed.

Among the mechanisms relying on overdense plasma, electron acceleration by resonantly excited relativistic surface plasma waves (SPWs) [7–13,25,26] has been demonstrated, leading to high charge, ultrashort bunches along the target surface, reaching energies largely above their quiver energy and correlated in time and space with extreme ultraviolet harmonic emission [10]. Advanced methods to control the duration and energy of the electron bunches have been proposed [12].

A compelling alternative, which draws attention by its seemingly simple concept, is the acceleration of electrons in the vacuum by a laser through straight energy transfer, known as vacuum laser acceleration [5,6,27–31]. Ideas to improve such a scheme have been proposed, like plasma mirror injectors [19,20], in which the electrons "surf" the reflected electromagnetic wave along a distance proportional to the Rayleigh length. The resulting bunches of nC charge reach energies of the order of MeV for a laser intensity $\sim 10^{19}$W/cm^2.

Alternatively, direct laser acceleration involves the nonresonant interaction of a laser with a solid target [5,21,22,32]. In particular, the use of a microstructured hollow-core target has been suggested that both guides and confines the laser pulse, resulting in an enhanced and superluminal longitudinal electric field [23,24].

II. ELECTRON ACCELERATION BY A DIFFRACTED FIELD

In this paper, an electron acceleration mechanism is unraveled that develops when an ultrahigh intensity p-polarized laser pulse irradiates the wedge of an overdense plasma target. We therefore propose an acceleration scheme that, considering an ultrashort ($\sim$25 fs), ultraintense ($\sim 10^{19}$ W/cm^2) laser pulse (assuming micrometric wavelengths), allows us to produce electron beams with hundreds of MeV energy, nC charge, and very small (a few degrees) angular aperture.

The scheme is depicted in Fig. 1, where the laser pulse propagates in the horizontal ($x > 0$) direction. It is focused onto the wedge of the target, where the latter consists of an overdense plasma slab occupying the regions $x > 0$ and $y < 0$ and extended over several laser wavelengths in the z direction.

Electron acceleration occurs at the ($y = 0$)−target surface which is irradiated by the laser at grazing incidence. In the following, we will identify the key role of the electromagnetic wave diffracted at the plasma wedge [see Fig. 1(b)] in accelerating the electrons. For a right-angle wedge, this diffracted wave propagates cylindrically, from the wedge outward, in all vacuum directions (from $\theta = 0$ to $\theta = 3\pi/2$). Most importantly, this wave carries a radial or longitudinal electric field which is responsible for the observed electron acceleration. This longitudinal field is maximum for small angles pointing in the direction of propagation of the incident laser, and it is shown to decay with the inverse square root of the distance from the wedge. We will demonstrate the effectiveness of this acceleration scheme capable of sustaining

---

[*] caterina.riconda@upmc.fr

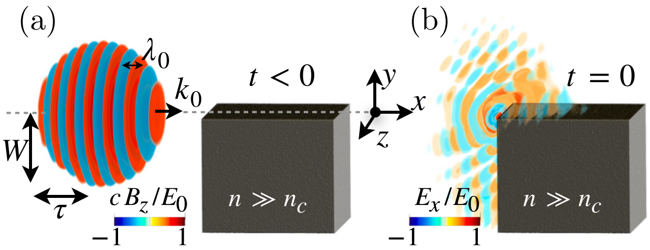

FIG. 1. (a) Laser-plasma interaction scheme. (b) Electric field E_x extracted from the 3D PIC simulation at the time $t = 0$, at which the normalized laser amplitude $a_0 = 5$ is maximum on the plasma edge (here $n = 100n_c$).

sub-mm acceleration lengths both through 3D particle-in-cell (PIC) simulations and through an analytical model showing that the electron energy increases with the square root of the acceleration distance and scales linearly with the laser maximum electric field amplitude.

III. 3D SIMULATIONS OF THE ELECTRON ACCELERATION AT THE WEDGE SURFACE

Simulations have been performed with the open source PIC code SMILEI [33]. In the simulations, the laser pulse has a maximum normalized vector potential $a_0 = eE_0/(m_e c\omega_0) = 5$ ($I\lambda_0^2 = 3.5 \times 10^{19}$ Wμm^2/cm^2, with I the laser intensity and λ_0 its wavelength) a Gaussian transverse profile with waist $\sigma_0 = 6\,\lambda_0$, duration $\tau = 8\,\lambda_0/c$ (full width at half maximum in intensity), and maximum electric field amplitude E_0. It is focused onto a cold plasma with electron density $n = 100\,n_c$, $n_c = \epsilon_0 m_e \omega_0^2/e^2$ being the critical density beyond which the plasma is opaque to an incident laser pulse with angular frequency $\omega_0 = 2\pi c/\lambda_0$ (ϵ_0 is the vacuum permittivity, m_e and $-e$ the electron mass and charge, respectively, and c the speed of light in vacuum). The details of the numerical set up are given in Appendix A. Figure 2 gives an example of a 3D simulation result. It reports in color scale the E_x component of the diffracted wave (normalized to E_0) at time $t = 18\lambda_0/c$, $t = 0$ denoting the time at which the maximum of the laser pulse reaches the edge of the target. In gray scale is the electron density. Electrons accelerated by the diffracted wave are clearly visible as bunches propagating with the longitudinal field, right above the target surface. The resulting electron energy spectrum is reported at different instants of time in Fig. 3(a), and the electron angular-energy distribution is reported at time $t = 54\lambda_0/c$ in Fig. 3(b), where $\phi_e = \arctan(p_y/p_x)$.

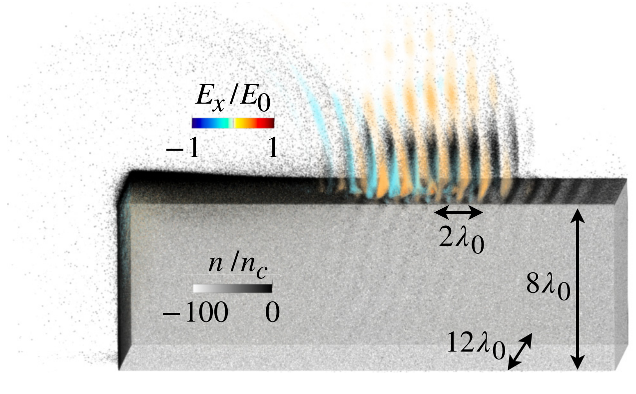

FIG. 2. Electric field E_x (in color, normalized to the maximum laser field strength E_0) and plasma density n/n_c (in gray scale) at $t = 18\lambda_0/c$. Results from the 3D PIC simulation with $a_0 = 5$ and $n = 100n_c$.

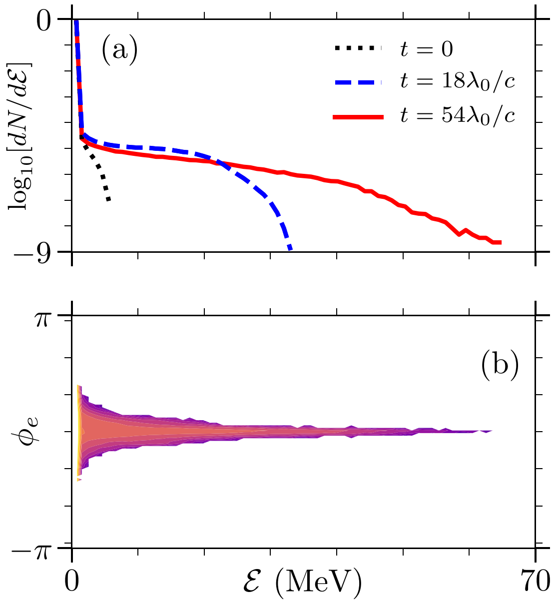

FIG. 3. (a) Electron energy ($\mathcal{E}$) spectrum at different times and (b) electron energy-angular distribution at $t = 54\lambda_0/c$. Results from the 3D PIC simulation with $a_0 = 5$ and $n = 100n_c$.

After only a few tens of optical cycles of interaction, the electrons have already reached energy of several tens of MeV, and carry substantial charges. When considering only electrons with energy above half the maximum energy (i.e., above 30 MeV at time $t = 54\lambda_0/c$) and assuming $\lambda_0 = 0.8\,\mu$m, we obtain a total charge of 0.8 nC, emitted within an angle ~80 mrad and normalized emittance $\epsilon_{n,\perp} \sim 4.5$ mm.mrad [34]. Similar charge levels were reported considering vacuum laser accelerators [19,23], but the present scheme allows us to obtain much higher electron energies at given laser intensity and duration.

IV. FIELDS IN THE WEDGE CONFIGURATION

Understanding how electrons are accelerated requires a deeper insight into the laser pulse diffraction at the plasma wedge, which can be drawn from previous theoretical [35,36] and numerical works [37]. In particular, the different electromagnetic field components are present in the electron acceleration region ($x > 0$, $y > 0$), and can be distinguished as (i) the incident electromagnetic wave, (ii) a (small amplitude) SPW propagating along with the vacuum-target interface, and (iii) the electromagnetic wave diffracted at the plasma wedge [35–37].

In the proposed scheme, electron acceleration is governed by the diffracted wave. A key element for efficient electron acceleration is that, due to the nonperfectly conducting nature of the plasma, the diffracted wave carries a nonzero radial

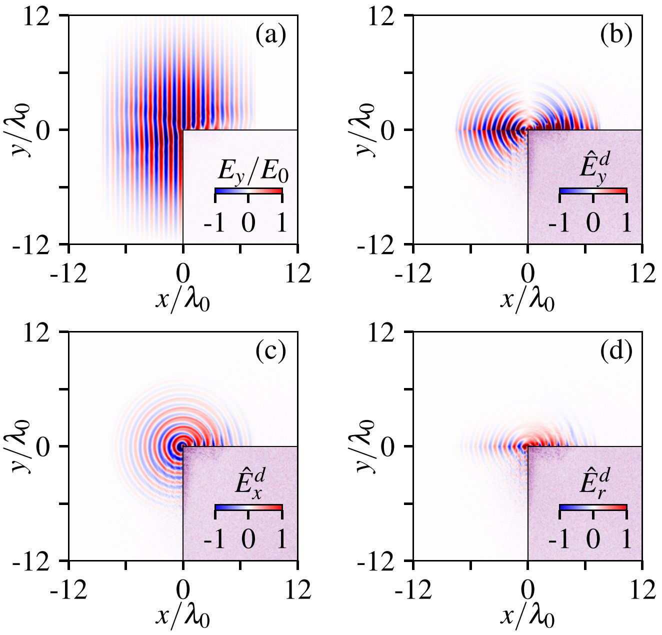

FIG. 4. Fields extracted from the 3D PIC simulation at $t = 0$: (a) total electric field E_y/E_0, (b) and (c) y and x components of the electric field associated to the diffracted wave, respectively, and (d) radial component of the electric field $\hat{E}_r^d$ associated to the diffracted wave.

or longitudinal electric field, maximum for diffraction angle $\theta \sim 0$, pointing along the target surface and thus efficiently accelerating particles in this direction. Unlike the SPW that is confined at the vacuum-target interface (within an evanescent length $\sim\lambda_0$), this longitudinal field of the diffracted wave extends over a few wavelengths in the ($x > 0, y > 0$) vacuum region. This property can be seen in Fig. 4, which reports different field components extracted from 3D PIC simulation for $a_0 = 5$ and $n = 100n_c$ at time $t = 0$ and for $z = 0$ (center of the laser pulse in the third dimension). Figure 4(a) depicts the total electric field E_y/E_0, (b) the E_y^d and (c) E_x^d components of the diffracted wave only, and (d) the radial component $E_r^d = \hat{E}_r^d\, e^{-i(\mathbf{k}.\mathbf{r}-\omega t)}$ of the diffracted wave, where $\hat{E}_r^d = \hat{E}_x^d(x/\sqrt{x^2+y^2}) + \hat{E}_y^d(y/\sqrt{x^2+y^2})$. All electric fields shown with a hat are reported in units of $m_e c\omega_0/e$.

To obtain the components of the diffracted field, we have run three different PIC simulations: (i) one in which the laser pulse is irradiated over the 3D plasma slab, resulting in the total field [Fig. 4(a)], (ii) one in which the laser pulse is irradiated over a plasma slab ($x > 0$ and $-\infty < y < \infty$) that blocks the whole laser beam and describes the reflected field, and (iii) one in which the laser pulse propagates in the free space and describes the incident wave. Then, for $y < 0$ ($y > 0$), we remove the incident (reflected) field from the total field. The field structures observed here are similar to those reported in the literature [35–37] considering the irradiation of a right-angled wedge by a plane wave. Our 3D PIC simulations confirm that even at relativistic intensities, and considering finite size and pulse duration, the diffracted field properties are preserved.

To perform parametric studies, we have considered a series of two-dimensional (2D) simulation at higher resolution (see details in Appendix A). The 2D simulations are representatives of the 3D fields at the center of the box (i.e., $z = 0$), and we found excellent agreement when benchmarking with the correspondent 3D cases (see Appendix B). For this reason, we will henceforth consider 2D PIC simulations in the following.

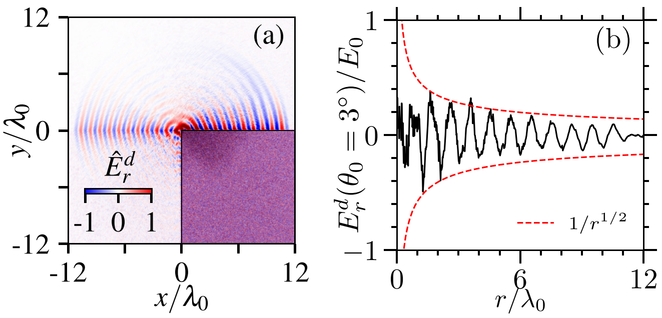

FIG. 5. 2D PIC simulation using a constant laser temporal profile. (a) Radial field $\hat{E}_r^d$ associated to the diffracted wave. (b) Line-out of $\hat{E}_r^d$ recorded at an angle $\theta_0 = 3^\circ$ from the target surface.

We reproduce in Fig. 5 the radial field from a 2D PIC simulation for which the laser field amplitude was kept constant over the whole simulation duration. This allows us to highlight the decrease with the distance from the wedge of the longitudinal field E_r close to the surface. The longitudinal field of the diffracted wave $\hat{E}_r^d$ is reported in Fig. 5(a), while Fig. 5(b) shows a line-out of the field recorded at a small angle $\theta_0 = 3^\circ$ with respect to the x direction (to remove noisy contributions at the surface location). The one-over-square-root dependence expected from Refs. [35–37] is recovered, and this slow decay can sustain the electron dynamics over long acceleration distances.

V. SCALING LAW FOR THE ELECTRON ACCELERATION

Because of the high directionality of the accelerated electrons reported in Fig. 3(b), we can consider the longitudinal electric field E_r of the diffracted wave, as the main driver for the electron acceleration, E_r is approximately equal to the E_x component. Based on these assumptions, a simple one-dimensional model can be derived to describe the electron acceleration process.

We consider that E_x decays in space as $1/\sqrt{k_0x}$ from its maximum value ηE_0 ($\eta \lesssim 1$ being the ratio of the maximum amplitude of the diffracted and the laser field that can be extracted from the simulations). The wave envelope and carrier are determined by the finite laser pulse itself. As a result, the equation of motion of an electron in the resulting longitudinal field reads

$$m_e\frac{d}{dt}\gamma v_x = -e\,\eta E_0\, e^{-(t-x/c)^2/\tau^2}\,\frac{\sin(k_0x-\omega_0t)}{\sqrt{k_0x}}, \tag{1}$$

where $v_x = dx/dt$ is the electron velocity and $\gamma = (1 - v_x^2/c^2)^{-1/2}$ its Lorentz factor. Equation (1) can be solved numerically considering a given initial position $x_0 = x(t = 0)$ and zero initial velocity $v_x(t = 0) = 0$. This equation can also be solved analytically for an ultrarelativistic electron, where $dt \sim dx/c$. In this limit, considering a constant phase and the peak field $-\eta E_0$, Eq. (1) reduces to $k_0^{-1}d\gamma/dx = \eta\, a_0/\sqrt{k_0x}$,

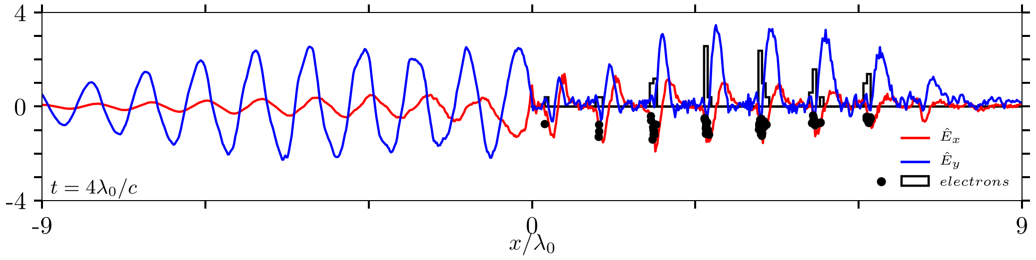

FIG. 6. Total transverse (blue) and longitudinal (red) electric fields at time $t = 4\lambda_0/c$ as extracted from a 2D simulation with $a_0 = 5$ and $n = 100n_c$. Black dots represent high energetic test electrons propagating with the wave and the solid black line is a histogram representing the number of accelerated electrons at a given position.

which leads to a scaling for the electron energy:

$$\gamma(t) \sim 2\eta a_0 \sqrt{\omega_0 t}. \qquad (2)$$

This scaling is found to be in excellent agreement with the maximum electron energy reported in Fig. 3(a), leading to maximum energies of 34 MeV ($\gamma \sim 67$) for $t = 18\lambda_0/c$ and 59 MeV ($\gamma \sim 116$) for $t = 54\lambda_0/c$ when taking $a_0 = 5$ and $\eta = 0.63$, which are consistent with our simulations. The square-root dependence of the electron energy with time is key evidence that the acceleration takes place in the longitudinal field of the diffracted wave.

VI. ELECTRON'S INJECTION

For electrons to be accelerated by the diffracted wave, they first need to be extracted from the plasma, then injected in the wave with a (longitudinal) velocity close to c so they can phase lock with the accelerating field. This early stage predominantly occurs *at the target wedge*, close to $x = 0$, where the laser transverse electric field, E_y, can efficiently pull electrons out of the plasma. This happens whenever E_y assumes negative values so the electrons acquire a positive transverse velocity $v_y > 0$. The resulting $v_y B_z$ contribution of the relativistic ($a_0 \gtrsim 1$) laser pulse together with the longitudinal $\sim E_x$ field of the diffracted wave can then bring the electron to near-relativistic longitudinal velocities ($v_x \sim c$) within less than an optical cycle. This happens above a threshold in the laser intensity ($a_0 > 1$) and inspection of particle orbits shows that, while both E_x and $v_y B_z$ contribute to the injection and phase locking, the first term dominates in most cases. Moreover, phase locking requires that the electrons are generated (extracted than injected) in a region where the longitudinal electric field of the diffracted wave is negative.

It is to be noted that as reported by Karal and Karp [36], the diffracted wave is not in phase with the incident laser wave, but phase-shifted by $5\pi/4$ with respect to it. This is confirmed in our PIC simulations and is visible when reporting the (total) longitudinal and transverse electric fields measured at the plasma surface, $y/\lambda_0 = 0$, as shown in Fig. 6. Indeed, electrons are injected at the plasma wedge, $x = 0$, when both $\hat{E}_x$ (solid red line) and $\hat{E}_y$ (solid blue line) are negative. Because of a phase shift of $5\pi/4$ between the E_y and E_r components for $x > 0$, electrons are injected once per laser period as nanobunches accelerating in the region of negative $\hat{E}_x$ field. In Fig. 6, the black dots represent high energetic test electrons propagating with the electromagnetic wave. The solid black line is a histogram representing the number of electrons at a given position. Once the particles phase lock, the total force due to the transverse fields is $\sim$0 and does not participate in the acceleration, as will be discussed more in detail in the following.

VII. VALIDATION OF THE SCALING LAW BY PIC SIMULATIONS

To confirm the validity of the model developed above and the interest of the proposed acceleration scheme, we report the results of a series of 2D PIC simulations in the x, y plane at longer timescales and for different laser intensities.

We first discuss in more detail the time evolution for our reference case $a_0 = 5$, whose results are summarized in Fig. 7. In Fig. 7(a), we report the temporal evolution of the Lorentz factor of three representative electrons (macroparticles) as they are accelerated in the diffracted wave. The Lorentz factor of the most energetic electron (red line) increases with time as predicted by our model (dashed line) [Eq. (1) using $\eta = 0.63$ and $x_0 = k_0^{-1}$], and shows strong evidence of the $\sqrt{\omega_0 t}$ time dependence. Note also that the Lorentz factor in this 2D simulation at times $t = 18\lambda_0/c$ ($\gamma \sim 65$) and $54\lambda_0/c$

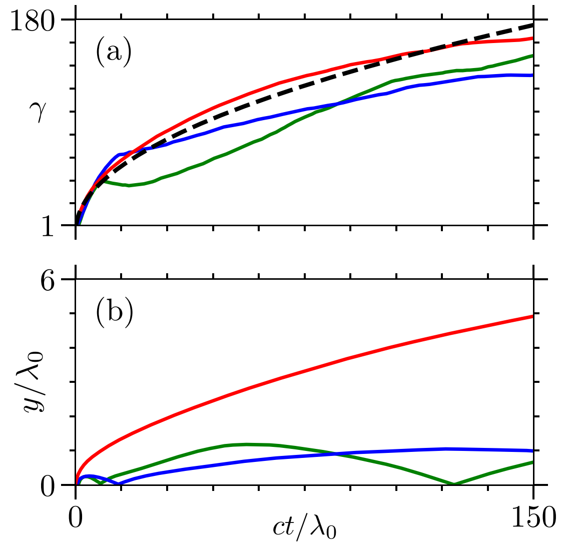

FIG. 7. (a) Temporal evolution of the Lorentz factor (γ) of three representative electrons extracted from 2D PIC simulations (with $a_0 = 5$ and $n = 100n_c$); the dashed black line is obtained by solving Eq. (1) numerically. (b) Transverse excursions of the three representative electrons shown in panel (a).

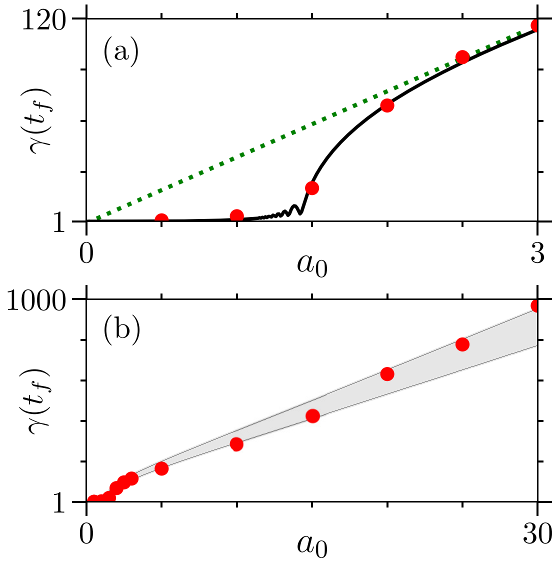

FIG. 8. Panels (a) and (b) report as red points the maximum Lorentz factor obtained in 2D PIC simulations at $t_f = 150\lambda_0/c$ as a function of a_0. In panel (a), the numerical integration of Eq. (1) is shown as a solid black line, and the prediction of Eq. (2) as a green dotted line (using $\eta = 0.63$). In panel (b), the grey region corresponds to the integration of Eq. (1) for $0.6 < \eta < 0.75$.

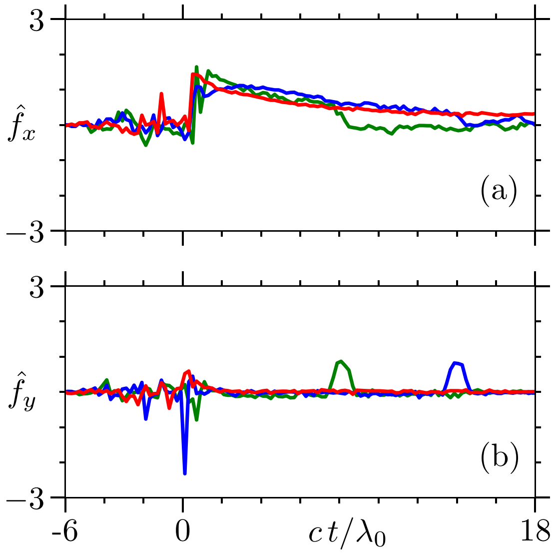

FIG. 9. Temporal evolution of (a) the parallel $\hat{f}_x = f_x/(m_e c\omega_0)$ and (b) the transverse $\hat{f}_y = f_y/(m_e c\omega_0)$ forces acting over the three electrons reported in Fig. 7.

($\gamma \sim 110$) is the same as in the 3D simulation. The blue and green lines correspond to electrons for which phase locking was less efficient, but that can later be picked up by the wave and further accelerated to large energies. For all these representative particles, our model gives a good estimate for the maximum energy (Lorentz factor) the particle can get as a function of time. This 2D simulation also shows that the acceleration can be maintained over long times, allowing us to reach high energies, here of the order of 86 MeV ($\gamma \sim 170$) at $t = 150\lambda_0/c$ for the most energetic electron (red line). The acceleration can thus develop over long distances along the target surface. As shown in Fig. 7(b), where we reproduce the trajectory of the same test particles as in Fig. 7(a), the electrons have propagated over $\sim 150\lambda_0$ in the x direction, but only a few wavelengths in the y direction (note the scale difference).

We then perform a scan in peak intensity from $I\lambda_0^2 \simeq 5.35 \times 10^{17}$ to 1.92×10^{21} W/cm^2, corresponding to a_0 in between 0.5 and 30, and assuming $\lambda_0 = 0.8\,\mu$m, while keeping the remaining laser and plasma parameters unchanged.

The maximum Lorentz factors achieved by an electron at time $t = 150\lambda_0/c$ was extracted as a function of a_0 and reported in Figs. 8(a) and 8(b). Figure 8(a) shows the transition of nonrelativistic to mildly relativistic field strengths, $0.5 \leqslant a_0 \leqslant 3$, where a threshold is clearly observed for $a_0 \sim 1.5$ (correspondingly, $\eta a_0 \sim 1$). The threshold is well reproduced by the theoretical model when solving Eq. (1) numerically (solid black line). The electron energy scaling given by Eq. (2) ($\propto a_0$, dashed green line), found by considering highly relativistic particles, gives excellent agreement with the PIC results above threshold. As a_0 increases, the parameter η shows a weak dependence with $a_0\, n_c/n$. In the simulations, we find that η is equal to 0.75 for $a_0 = 30$. Indeed, as shown in Fig. 8(b), the energy scaling using $\eta = 0.75$ in Eq. (1) gives a better estimate at large a_0.

The agreement between the simulations and our one-dimensional model can be understood by looking at the forces acting on the accelerated electrons. The longitudinal [$f_x = -e(E_x + v_y B_z)$] and perpendicular [$f_y = -e(E_y - v_x B_z)$] forces experienced by the three electrons discussed in Fig. 7 are reported in Figs. 9(a) and 9(b), respectively, for our reference case. For readability, only short times $t < 18\lambda_0/c$ are shown. The longitudinal force f_x in Fig. 9(a) clearly shows the $1/\sqrt{\omega_0 t}$ time dependence expected for acceleration in the longitudinal field of the diffracted wave (with $ct \sim x$). This confirms the dominant contribution of E_x compared to the magnetic force $v_y B_z$ (consistent with the fact that v_y stays small for the high-energy electrons and that the energy gain is due to the work of the longitudinal field only). From Fig. 9(b), we also see that the transverse force f_y experienced by the electron is always very small, which implies that the two contributions E_y and $v_x B_z$ compensate each other (which is possible for $v_x \to c$). The transverse force assumes non-negligible values only at the time of injection ($t \sim 0$) and for the electron represented by the green and blue lines, at times $t \sim 8\lambda_0/c$ and $15\lambda_0/c$, respectively. A closer look at the particle orbits shows that these times correspond to the moment when those particles are bouncing off the target surface. Indeed, at those times the electrons penetrate the plasma skin depth, experience a screened electric field ($E_y \to 0$), and are turned back by the strong $v_x B_z$ force (B_z is not screened). At those times, the electrons do not gain energy [see Fig. 7(a)], but they can re-enter the wave and get further accelerated.

VIII. PHASE LOCKING

The slow decrease ($\propto 1/\sqrt{k_0 x}$) of the longitudinal field of the diffracted wave along the target surface means that electrons can, in principle, remain in phase and be accelerated over distancesor times even longer that that considered so far.

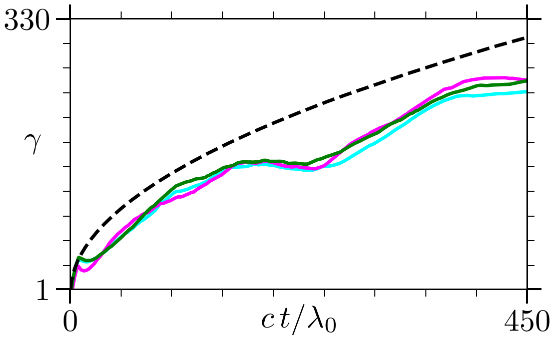

FIG. 10. Temporal evolution of the Lorentz factor (γ) of three electrons which are accelerated over a long time interval. The dashed black line is the result from the theoretical approach using $\eta = 0.63$. The green line represents the same particle in all panels. Here, $a_0 = 5$ and $n = 100n_c$.

This is confirmed in Fig. 10, where few selected high-energy electrons from our reference case were tracked over 450 optical cycles, propagating distances $\sim 450\lambda_0$ along the target surface and reaching energies of nearly 130 MeV ($\gamma \sim 260$).

To explain this, we examine the phase shift an electron acquires with respect to the accelerating wave:

$$\Delta\varphi = k_0 \int_{t_{\text{inj}}}^{t} (c - v_x)\, dt. \tag{3}$$

For relativistic electrons, $v_x(t)$ is well approximated by Eq. (2) [using $v_x = (1 - 1/\gamma^2)^{1/2}$]. In addition, if we assume that the electron energy at time t is much larger than that at the moment of injection [$\gamma(t) \gg \gamma(t_{\text{inj}})$], then we obtain that the phase shift $\Delta\varphi \sim (8\eta^2 a_0^2)^{-1} \ln 4\eta^2 a_0^2\, \omega_0 t$ increases logarithmically with time. Conversely, the dephasing time $\omega_0 t_d \propto \exp(8\pi\eta^2 a_0^2)$, at which $\Delta\varphi \sim \pi$, increases exponentially with $\eta^2 a_0^2$. This ensures that the electron can remain in phase with the accelerating field whenever $\eta a_0 > 1$.

Considering the forces in Figs. 9(a) and 9(b), the transverse motion in the complex field resulting from the superposition of the cylindrical diffracted wave and incident laser field can induce in some particles a temporary dephasing with respect to the accelerating field as they hit the surface. A similar effect can occur at much longer timescales, and it is at the origin of the fact that for a short amount of time the energy stops increasing, as visible in Fig. 10, but starts again after reinjection. Note also that 3D diffraction effects can set in over long distances and limit the acceleration.

IX. ROLE OF THE PLASMA DENSITY

As discussed earlier, we find a very weak dependence of the amplitude of the diffracted wave that is represented by the η parameter with $a_0 n_c/n$. Complementary simulations with different plasma densities also show that both the η parameter and the final electron acceleration are almost independent of n/n_c, as long as it is much larger than one. Moreover, the diffracted wave phase velocity should be independent of the plasma density. This is in contrast with SPWs, whose phase velocity, as predicted from the theory $v_{\text{ph}} \approx c(1 - n_c/2n)$ [8] depends on the parameter n/n_c and is subluminal. We exploited this result to show that, even if a surface plasma is present, the main contribution to acceleration comes from the diffracted wave.

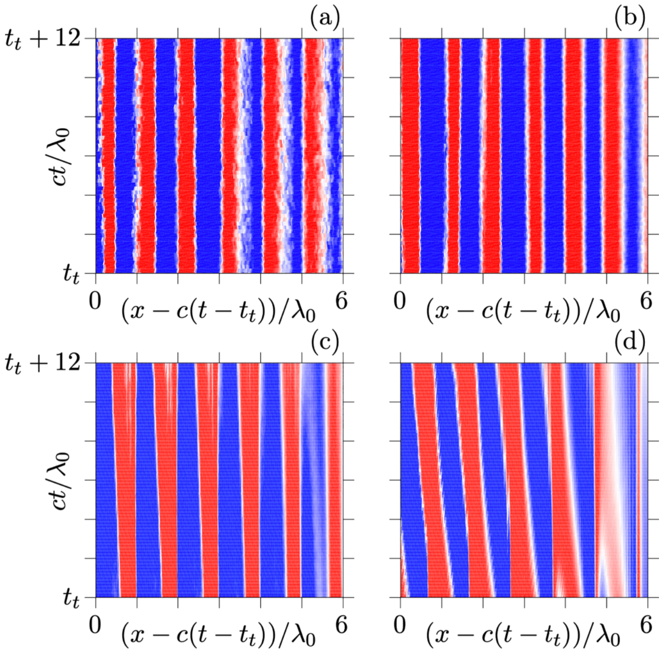

FIG. 11. Field phase velocity observed from two different setups: the one in the present paper, panels (a) and (b), and a setup involving resonant excitation of surface plasma waves, as in Ref. [12], with $\Delta\beta = 0$ and $\theta_{\text{inc}} = 31^\circ$, panels (c) and (d). In the figures, $a_0 = 5$ and $t_t = 30c/\lambda_0$ is much longer than the pulse duration.

We measured the temporal evolution of the longitudinal electric field amplitude (represented by the saturated colors) in our configuration in a frame that moves at the speed of light using a probe located on the plasma surface. The vertical lines indicate no variation in the phase velocity, both for the case the plasma density is $n = 100n_c$ in Fig. 11(a) and $n = 20n_c$ in Fig. 11(b). We then performed simulations where we resonantly excite SPWs (same arrangement as Ref. [12] with $\Delta\beta = 0$ and $\theta_{\text{inc}} = 31^\circ$). In contrast to the previous case, we observe with the same diagnostic that the wave phase velocity depends on the density: it is slightly less, but the same order than c for $n = 100n_c$ as shown in Fig. 11(c) and clearly smaller then the speed of light, $v_{\text{ph}} \approx 0.96c$, for the lower density case $n = 20n_c$, Fig. 11(d), as expected.

We also note that the excursion of the electrons shown in Fig. 7(b) show that efficient electron acceleration can happen at some wavelengths above the surface. This indicates that resonant SPWs are not at the origin of the particle acceleration as these waves are well localized at the target surface and decay exponentially with the distance from the surface over evanescent lengths of the order of λ_0.

X. DISCUSSION AND CONCLUSION

The robustness of the proposed acceleration mechanism was tested using complementary 2D PIC simulations (not shown). In these simulations, various parameters were changed, such as the shape of the target's corner or the roughness of the plasma surface. The presence of a small preplasma

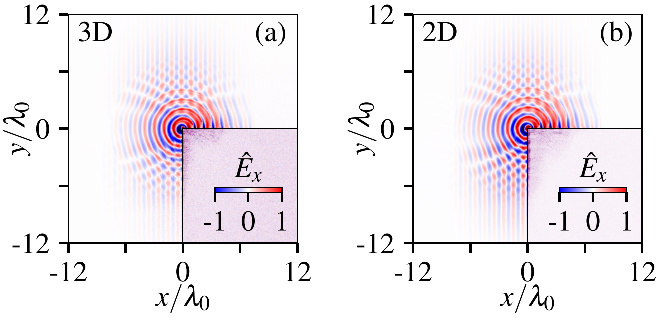

FIG. 12. Comparison of the total field $\hat{E}_x$ extracted from (a) 3D and (b) 2D simulations.

or a small misalignment of the laser were also considered (the laser impinging at an angle up to ±5° with respect to the surface, and with variations of the focus location of a few wavelengths in all directions). In all these complementary simulations, the parameter η and the electron acceleration was shown to be marginally impacted, suggesting that this acceleration scheme could be easily implemented in experiments aimed at demonstrating new energetic particle sources. Moreover, the laser transverse size and pulse duration can be used to control the total charge: the longer the pulse, the more electron bunches will be accelerated. We verified this trend by performing 3D PIC simulations increasing either the transverse size by one and a half or doubling the pulse duration. In the first case, we found an increase of 76% of the charge, and in the second case the doubling of the charge for the 30% fastest particles. However, the increase of the charge with the laser pulse will likely be limited by the plasma evolution for pulses above a few 100 fs range. A consequence of the robustness of this acceleration mechanism is that, even though it was never identified or discussed in previous works, acceleration in the field of the diffracted could develop in various laser-plasma interaction setups.

In conclusion, a unique mechanism of electron acceleration has been identified in the interaction of a relativistically intense laser pulse with an overdense plasma wedge. Both 3D and 2D PIC simulations have shown this mechanism to be robust and provide highly charged (nC), well-collimated electron bunches with energies of several tens to hundreds of MeV. A simple analytical model has been developed that shows that the maximum energy of the accelerated electrons scales linearly with the laser field strength parameter (a_0) and increases with the square root of time to values well beyond the ponderomotive scaling. From this model, we obtain that the particle energy gain can be controlled by the longitudinal target size and, in particular, that the maximum electron energy scales with the square root of this size. As for the total charge of the accelerated beam, it can be controlled by the laser transverse size and pulse duration.

Note added. Recently, we came across a study by Shen *et al.* [38,39] where the authors report on electron acceleration along a thin film irradiated at parallel incidence by an intense laser. While they attribute electron acceleration to the excitation of a SPW, our results suggest that they should also consider acceleration in the diffracted wave. A similar scheme was also proposed by Sarma *et al.* [40] with emphasis on SPW excitation.

ACKNOWLEDGMENTS

P.S.K. was supported by the CEA NUMERICS program, which has received funding from the European Union's Horizon 2020 research and innovation program under the Marie Sklodowska-Curie Grant Agreement No. 800945. Financial support from Grant No. ANR-11-IDEX-0004-02 Plas@Par is acknowledged. Simulations were performed on the Irene-SKL machine hosted at TGCC- France, using High Performance Computing resources from GENCI-TGCC (Grant No. 2021-x2016057678). The authors are grateful to F. Amiranoff, A. Grassi, F. Massimo, A. Mercuri, F. Pérez, L. Romagnani, and T. Vinci for fruitful discussions and to the SMILEI dev-team for technical support.

APPENDIX A: NUMERICAL SETUP

Simulations have been performed with the SMILEI PIC code [33]. The 3D simulation box is $72\lambda_0 \times 24\lambda_0 \times 24\lambda_0$ (in the x-y-z directions) and composed of $4608 \times 1536 \times 1536$ cells (spatial resolution $\Delta = \lambda_0/64$). The time resolution is $\Delta t = 0.95\Delta/(\sqrt{3}c)$. Electromagnetic field boundary conditions are injecting or absorbing in the x direction and absorbing in the y, z directions. Particle boundary conditions are either thermalizing at $y_{\min}$, $z_{\min}$, and $x_{\max}$ or absorbing in complementary directions. In each computational plasma cell, there are four macroelectrons and four macroions. The ion over electron mass ratio is given by $A\,m_p/Z = 1836\,m_e$, with A, Z, respectively, the atomic number and charge, and m_p the proton mass.

The 2D simulation box is $192\lambda_0 \times 36\lambda_0$ (in the x, y directions) and composed of 49152×9216 cells (spatial resolution $\Delta = \lambda_0/128$). The time resolution is $\Delta t = 0.95\Delta/(\sqrt{2}c)$. In each computational plasma cell, there are 32 macroelectrons and 32 macroions. The electromagnetic field and particle boundary conditions are the same as in the 3D simulation.

APPENDIX B: 2D AND 3D SIMULATION COMPARISON

The same electromagnetic field structures are recovered in 2D PIC simulations using the same physical (laser and plasma) parameters, but with higher resolution, box size, and duration of the simulation. A direct comparison of the $\hat{E}_x$ component of the electric field drawn from 3D and 2D PIC simulations is reported in Fig. 12. The two simulations show excellent agreement, and we verified that the same is true for the other fields. A 3D simulation with reduced resolution (not shown) also confirms that both the general electromagnetic field structure and the electron acceleration were correctly described in 2D simulations up to the maximum time accessible in the 3D simulation $t \sim 150\lambda_0/c$.

---

[1] D. C. Joy, and B. G. Frost, Scanning electron microscopy: Present capability, future improvements and potential replacements, AIP Conf. Proc. **550**, 561 (2001).

[2] S. V. Bulanov, J. J. Wilkens, T. Zh. Esirkepov, G. Korn, G. Kraft, S. D. Kraft, M. Molls, and V. S. Khoroshkov, Laser ion acceleration for hadron therapy, Phys. Usp. **57**, 1149 (2014).

[3] I. Levchenko, S. Xu, S. Mazouffre, D. Lev, D. Pedrini, D. Goebel, L. Garrigues, F. Taccogna, and K. Bazaka, Perspectives, frontiers, and new horizons for plasma-based space electric propulsion, Phys. Plasmas **27**, 020601 (2020).

[4] E. Esarey, C. B. Schroeder, and W. P. Leemans, Physics of laser-driven plasma-based electron accelerators, Rev. Mod. Phys. **81**, 1229 (2009).

[5] N. Naumova, I. Sokolov, J. Nees, A. Maksimchuk, V. Yanovsky, and G. Mourou, Attosecond Electron Bunches, Phys. Rev. Lett. **93**, 195003 (2004).

[6] N. Naumova, J. A. Nees, and G. A. Mourou, Relativistic attosecond physics, Phys. Plasmas **12**, 056707 (2005).

[7] M. Raynaud, J. Kupersztych, C. Riconda, J. C. Adam, and A. Heron, Strongly enhanced laser absorption and electron acceleration via resonant excitation of surface plasma waves, Phys. Plasmas **14**, 092702 (2007).

[8] C. Riconda, M. Raynaud, T. Vialis, and M. Grech, Simple scalings for various regimes of electron acceleration in surface plasma waves, Phys. Plasmas **22**, 073103 (2015).

[9] A. MacchiSurface plasmons in superintense laser-solid interactions, Phys. Plasmas **25**, 031906 (2018).

[10] G. Cantono, L. Fedeli, A. Sgattoni, A. Denoeud, L. Chopineau, F. Réau, T. Ceccotti, A. Macchi *et al.*, Extreme Ultraviolet Beam Enhancement by Relativistic Surface Plasmons, Phys. Rev. Lett. **120**, 264803 (2018).

[11] M. Raynaud, A. Heron, and J.-C. Adam, Excitation of surface plasma waves and fast electron generation in relativistic laser-plasma interaction, Sci. Rep. **10**, 13450 (2020).

[12] S. Marini, P. S. Kleij, F. Pisani, F. Amiranoff, M. Grech, A. Macchi, M. Raynaud, and C. Riconda, Ultrashort high energy electron bunches from tunable surface plasma waves driven with laser wavefront rotation, Phys. Rev. E **103**, L021201 (2021).

[13] S. Marini, P. S. Kleij, F. Amiranoff, M. Grech, C. Riconda, and M. Raynaud, Key parameters for surface plasma wave excitation in the ultra high intensity regime, Phys. Plasmas **28**, 073104 (2021).

[14] O. Lundh, J. Lim, C. Rechatin, L. Ammoura, A. Ben-Isma'l, X. Davoine, G. Gallot, J-P. Goddet, E. Lefebvre, V. Malka, and J. Faure, Few femtosecond, few kiloampere electron bunch produced by a laser-plasma accelerator, Nat. Phys. **7**, 219 (2011).

[15] M. Bailly-Grandvaux, D. Kawahito, C. McGuffey, J. Strehlow, B. Edghill, M. S. Wei, N. Alexander, A. Haid, C. Brabetz, V. Bagnoud, R. Hollinger, M. G. Capeluto, J. J. Rocca, and F. N. Beg, Ion acceleration from microstructured targets irradiated by high-intensity picosecond laser pulses, Phys. Rev. E **102**, 021201(R) (2020).

[16] A. R. Knyazev, Y. Zhang, and S. I. Krasheninnikov, Laser-driven electron acceleration in nanoplate array targets, Phys. Rev. E **103**, 013204 (2021).

[17] B. Quesnel and P. Mora, Theory and simulation of the interaction of ultraintense laser pulses with electrons in vacuum, Phys. Rev. E **58**, 3719 (1998).

[18] S. Marini, E. Peter, G. I. de Oliveira, and F. B. Rizzato, Breakdown of the ponderomotive approximation as an acceleration mechanism in wave-particle nonlinear dynamics, Phys. Plasmas **24**, 093113 (2017).

[19] M. Thévenet, A. Leblanc, S. Kahaly, H. Vincenti, A. Vernier, F. Quéré, and J. Faure, Vacuum laser acceleration of relativistic electrons using plasma mirror injectors, Nat. Phys. **12**, 355 (2016).

[20] C. Zhou, Y. Bai, L. Song, Y. Zeng, Y. Xu, D. Zhang, X. Lu, Y. Leng, J. Liu, Y. Tian, R. Li, and Z. Xu, Direct mapping of attosecond electron dynamics, Nat. Photonics **15**, 216 (2021).

[21] M. Wen, Y. I. Salamin, and C. H. Keitel, Electron Acceleration in Direct Laser-Solid Interactions Far Beyond the Ponderomotive Limit, Phys. Rev. Appl. **13**, 034001 (2020).

[22] A. V. Arefiev, A. P. L. Robinson, V. N. Khudik, Novel aspects of direct laser acceleration of relativistic electrons, J. Plasma Phys. **81**, 475810404 (2015).

[23] K. D. Xiao, T. W. Huang, L. B. Ju, R. Li, S. L. Yang, Y. C. Yang, S. Z. Wu, H. Zhang, B. Qiao, S. C. Ruan, C. T. Zhou, and X. T. He, Ion acceleration from microstructured targets irradiated by high-intensity picosecond laser pulses, Phys. Rev. E **93**, 043207 (2016).

[24] Z. Gong, A. P. L. Robinson, X. Q. Yan, and A. V. Arefiev, Highly collimated electron acceleration by longitudinal laser fields in a hollow-core target, Plasma Phys. Control. Fusion **61**, 035012 (2019).

[25] L. Willingale, A. G. R. Thomas, P. M. Nilson, H. Chen, J. Cobble, R. S. Craxton, A. Maksimchuk, P. A. Norreys, T. C. Sangster, R. H. H. Scott, C. Stoeckl, C. Zulick, and K. Krushelnick, Surface waves and electron acceleration from high-power, kilojoule-class laser interactions with underdense plasma, New J. Phys. **15**, 025023 (2013).

[26] L. Fedeli, A. Sgattoni, G. Cantono, D. Garzella, F. Réau, I. Prencipe, M. Passoni, M. Raynaud, M. Květoň, J. Proska, A. Macchi, T. Ceccotti, Electron Acceleration by Relativistic Surface Plasmons in Laser-Grating Interaction, Phys. Rev. Lett. **116**, 015001 (2016).

[27] E. Esarey, P. Sprangle, and J. Krall, Laser acceleration of electrons in vacuum, Phys. Rev. E **52**, 5443 (1995).

[28] F. Hartemann, S. Fochs, G. Le Sage, N. Luhmann, J. Woodworth, M. Perry, Y. Chen, and A. Kerman, Nonlinear ponderomotive scattering of relativistic electrons by an intense laser field at focus, Phys. Rev. E **51**, 4833 (1995).

[29] J. Pang, Y. K. Ho, X. Q. Yuan, N. Cao, Q. Kong, P. X. Wang, L. Shao, E. H. Esarey, and A. M. Sessler, Subluminous phase velocity of a focused laser beam and vacuum laser acceleration, Phys. Rev. E **66**, 066501 (2002).

[30] J. F. Hua, Y. Z. Lin, Ch. X. Tang, Y. K. Ho, and Q. Kong, Phase motion of accelerated electrons in vacuum laser acceleration, J. Appl. Phys. **101**, 023102 (2007).

[31] P. K. Singh, F.-Y. Li, C.-K. Huang, A. Moreau, R. Hollinger, A. Junghans, A. Favalli, C. Calvi, S. Wang, Y. Wang, H. Song, J. J. Rocca, R. E. Reinovsky and, S. Palaniyappan, Vacuum laser acceleration of super-ponderomotive electrons using relativistic transparency injection, Nat. Commun. **13**, 54 (2022).

[32] M. Jirka, M. Vranic, T. Grismayer, and L. O. Silva, Scaling laws for direct laser acceleration in a radiation-reaction dominated regime, New J. Phys. **22**, 083058 (2020).

[33] J. Derouillat, A. Beck, F. Pérez, T. Vinci, M. Chiaramello, A. Grassi, M. Flé, G. Bouchard, I. Plotnikov, N. Aunai, J. Dargent, C. Riconda, and M. Grech, Smilei: A collaborative, open-source, multi-purpose particle-in-cell code for plasma simulation, Comput. Phys. Commun. **222**, 351 (2018).

[34] M. Ferrario, *Injection, Extraction and Matching*, Proceedings of the CAS-CERN (CERN, Geneva, 2016).

[35] C. A. Balanis, *Advanced Engineering Electromagnetics*, 2nd ed. (John Wiley & Sons, Inc., Hoboken, NJ 07030, USA, 2012).

[36] F. C. Karal Jr., and S. N. Karp, Diffraction of a plane wave by a right angled wedge which sustains surface waves on one face, Quart. Appl. Math. **20**, 97 (1962).

[37] Y. Xi, Y. S. Jung, and H. K. Kim, Interaction of light with a metal wedge: The role of diffraction in shaping energy flow, Opt. Express **18**, 2588 (2010).

[38] X. F. Shen, A. M. Pukhov, S. E. Perevalov, and A. A. Soloviev, Electron acceleration in intense laser - solid interactions at parallel incidence, Quantum Electron. **51**, 833 (2021).

[39] X. F. Shen, A. Pukhov, and B. Qiao, Monoenergetic High-Energy Ion Source via Femtosecond Laser Interacting with a Microtape, Phys. Rev. X **11**, 041002 (2021).

[40] J. Sarma, A. McIlvenny, N. Das, M. Borghesi, and A Macchi, Surface plasmon-driven electron and proton acceleration without grating coupling, New J. Phys. **24**, 073023 (2022).

Correction: The affiliation indicators for the third, fourth, and fifth authors were incorrect and have been fixed.